Powder Technology 428 (2023) 118798

Contents lists available at ScienceDirect

Powder Technology

journal homepage: www.journals.elsevier.com/powder-technology

The effect of relative humidity on deposition pattern in inertial impactors: The role of particle elasticity and surface attraction

S. Kala *, J.R. Saylor

Department of Mechanical Engineering, Clemson University, Clemson, SC, USA

HIGHLIGHTS

- Novel technique for understanding particle-surface interactions.
- Peak particle deposition locations independent of relative humidity.
- Secondary particle deposits or 'halos' occur when relative humidity low.
- Particle bounce responsible for formation of secondary deposits.
- Hamaker constant and coefficient of restitution are related to relative humidity.

GRAPHICAL ABSTRACT

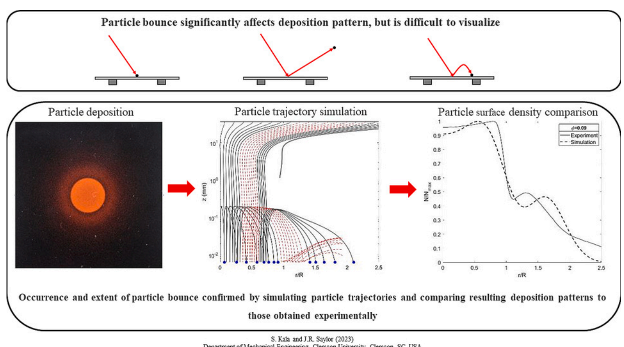

ARTICLE INFO

Keywords:
Particle bounce
Hamaker constant
Coefficient of restitution
Relative humidity
Secondary deposits
Halos

ABSTRACT

The role of relative humidity on particle bounce in an inertial impactor was investigated through a program of experiments and particle trajectory simulations. Inertial impactors are devices used to obtain particle size distributions by passing particle-laden air through a nozzle and collecting particles having sufficient inertia on a flat surface placed directly below the nozzle. Herein monodisperse hygroscopic particles impacted the flat hydrophobic surface of a single stage inertial impactor while varying the relative humidity of the flow. The results show that a circular deposition pattern occurs when the relative humidity is high. When the relative humidity is low secondary deposits beyond the circular deposit also occur. Particle trajectory simulations were performed where particle/surface interactions were quantified via the Hamaker constant (A) and the loss of kinetic energy via the coefficient of restitution (e). In a first-of-its-kind approach, (A, e) were iteratively adjusted until prominent features of the particle deposits in the experiments and simulations agreed, thereby providing values of (A, e) for each relative humidity. The results show that the observed deposition behavior is due to (i) the increase with relative humidity of the repulsion between the hygroscopic particles and the hydrophobic surface, (ii) multiple bounces along the particle trajectory, and (iii) kinetic energy loss at each particle bounce.

* Corresponding author.
E-mail addresses: skala@clemson.edu (S. Kala), jsaylor@clemson.edu (J.R. Saylor).

https://doi.org/10.1016/j.powtec.2023.118798
Received 2 May 2023; Received in revised form 24 June 2023; Accepted 7 July 2023
Available online 10 July 2023

1. Introduction

Inertial impactors are used for measuring particle size distributions in air for diameters ranging from as low as 0.005 μm [1] to as large as 100 μm [2] and are used under a variety of operating conditions [3]. Impactors have been used in underground mine studies [4], in atmospheric pollution studies [5], in visibility studies [6], and for monitoring bioaerosols in order to control air quality and estimate performance of air cleaning devices [7]. They have also been used extensively in experimental research [8–11].

A typical inertial impactor, a schematic of which is shown in Fig. 1, consists of a nozzle through which a particle laden flow enters and creates a very short jet that is directed at an impaction plate or substrate. Large particles which have sufficient inertia will depart the flow streamlines and collect on the impaction plate whereas small particles follow the streamlines, are not deposited, and are collected at a subsequent impactor stage. There are three possible fates for a particle that impacts the plate: (a) the particle may deposit, (b) the particle may bounce on impact after which it is transported out of the impactor, and (c) the particle may bounce on impact and then deposit at another location. These three possibilities are shown schematically in Fig. 2. It is possible that scenario (c) may occur more than once followed by either (a) or (b). We note that yet another possibility exists wherein particles, once deposited on the plate, slide laterally outward by shear at the wall, however this possibility is not explored herein.

Particle bounce can cause inaccuracies in the particle size distribution obtained by impactors [11]. Specifically, particle bounce can cause a decrease in collection efficiency, increased wall losses, and altered collection distributions among stages [10]. A physical understanding of the factors that control the bounce and potential reimpaction of particles is therefore critical to the prediction of impactor performance, as well as to the design of more accurate impactors and development of better measurement conditions for impactor operation.

Particle bounce has been discussed extensively in the literature [12–19] and numerous methods to arrest particle bounce have been suggested, the majority of which advocate the use of coated impaction plates. An increase in particle collection by coating impaction surfaces with petroleum jelly, paraffin, silicone oil, Apiezon L, and other adhesive materials has been reported in previous studies on particle bounce [13,20,21]. These studies suggest that coating leads to a decrease in particle bounce, evidenced by increases in particle collection efficiency. However, these studies do not state whether these coatings promote scenario (a) or (c) in Fig. 2. This information becomes necessary when attempting to explain the particle deposition patterns observed on collection plates, which will be discussed later, as well as designing impactors to arrest bounce completely.

Since coated slides cannot be used in all particle impactor studies, for example where the impactor samples must be used for chemical analysis [22], alternate methods to arrest particle bounce in impactors have been proposed. For instance, it has been reported that particle collection in impactors with uncoated slides can be increased by simply increasing the relative humidity of the flow. This was shown by Stein et al. [23] who studied the effect of relative humidity on particle bounce for uncoated aluminum plates. His study revealed that as the relative humidity increased from 0% to 80%, the particle collection efficiency increased, suggesting a decrease in particle bounce. Wang & John [15] observed a 25% increase in collection efficiency when the relative humidity increased from 17% to 64% using uncoated stainless steel impaction plates. These results are similar to those obtained by Winkler [22] who also used uncoated substrates to collect atmospheric aerosols at different relative humidities. The present understanding, based on the above studies, is that with increase in relative humidity, particles adsorb water on their surface, making them “less bouncy” [23] and that, therefore, they adhere to the surface. However, precisely what physical processes are controlling the deposition is not revealed. Also, as with the case of using coated surfaces to control particle bounce, it is not clear whether particle bounce is completely arrested when relative humidity is increased, leading to scenario (a) in Fig. 2 or if something like scenario (c) occurs instead.

The substrates used by Stein et al. [23] and Wang & John [15] in their study of the effect of relative humidity on particle bounce were aluminum plates and stainless steel plates, respectively which are relatively hydrophilic in nature. This is important because the relative humidity affects the amount of water adsorbed on the surface of a particle, and so the hydrophobic or hydrophilic nature of the impactor surface should influence the adhesion of such particles with the surface and show a difference in particle bounce behavior. The significance of this point is supported by results obtained from static studies of adhesion of different surfaces using atomic force microscopy (AFM) which show (not surprisingly) that the adhesion force of a surface increases with relative humidity for a hydrophilic surface while it decreases for a hydrophobic surface [24–27]. Hence, previous studies on the effect of relative humidity during particle impaction in impactors have not captured the entire scope of the problem by ignoring the effect of surface hydrophobicity/hydrophilicity on particle bounce.

Apart from collection efficiency, another characteristic of particle impactors which has been attributed to particle bounce is the pattern of particle deposition, specifically the existence of secondary deposits on the impactor surface. Ideally the impaction pattern in a particle impactor is a disk having a diameter roughly equal to that of the nozzle, and which lacks any secondary deposits outside of the disk. An example of such an ideal pattern is shown in Fig. 3. Such patterns are what is expected for typical impactor operation. But secondary deposits outside the disk have been observed; such patterns are often referred to as halos [28–30]. Oodo et al. [29] claimed that particle bounce was the cause of secondary deposits observed on uncoated glass slides; no secondary deposits were found on silicon grease coated glass slides for the same particles and impactor conditions. Soysal et al. [30] attributed secondary deposits to the particles bouncing off the impaction plate directly below the nozzle (presumably any radial location less than or equal to the nozzle radius which they regarded as the “primary impaction zone”) by comparing the collection efficiency of the primary impaction zone to the overall collection efficiency of the plate for different particle sizes. Both Oodo et al. [29] and Soysal et al. [30] attribute the secondary deposit formation to particle bounce on the impaction plate directly below the nozzle followed by reimpaction and collection on the impaction plate at a radial location exceeding the nozzle radius. However, neither author provides a physical mechanism explaining why particles bounce, re-impact, and deposit at an outer radial location or why particles bounce at radial locations less than the nozzle radius but don’t bounce upon reimpaction at radial locations exceeding the nozzle radius.

Finally, though it is often implied that the disk has a uniform particle

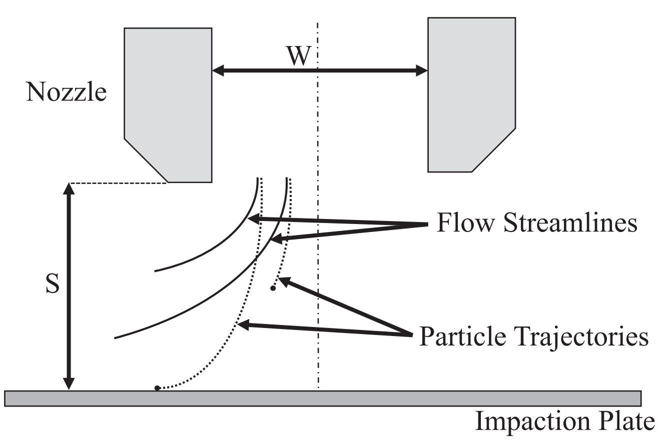

Fig. 1. Schematic of an inertial impactor. The nozzle diameter is W and the nozzle-to-plate distance is S.

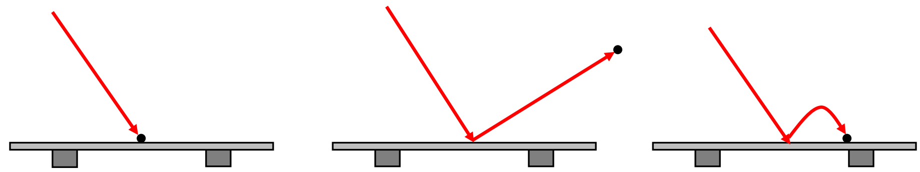

Fig. 2. Particle impaction possibilities: (a) the particle impacts and collects at the impaction point; (b) the particle bounces and is transported out of the impactor without collection; (c) the particle bounces upon impact and then deposits at another location.

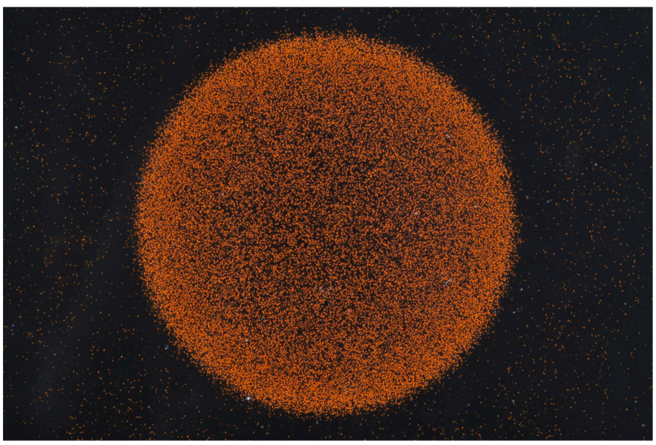

Fig. 3. Image of a standard impactor pattern. Here, the ratio of the nozzle-to-plate distance to the nozzle diameter $S/W = 1$, and the pattern diameter and nozzle diameter are 12.7 mm. The particle diameters here were 12.4 μm.

surface density, this density can vary with radius, and it is possible that bounce affects this variation. Sethi & John [31] observed non uniform particle surface density for disk shaped deposits when impacting 3 μm ammonium fluorescein particles on petroleum jelly coated aluminum surfaces. The surface density was observed to be minimum at the nozzle axis, increasing towards the nozzle edge and reaching a maximum value before falling steeply at the edge of the disk. Such behavior is also seen in Fig. 3. The radial location for the peak particle surface density was observed to decrease with particle Stokes number

$$Stk = \frac{\rho d^2 u}{9\mu W}, \tag{1}$$

where ρ is the particle density, u is the nozzle exit velocity, d is the particle diameter, μ is the dynamic viscosity of air, and W is the nozzle diameter. The peak surface density moved from the nozzle edge for $\sqrt{Stk} = 0.5$ to roughly 0.3 times the nozzle radius for $\sqrt{Stk} = 1.6$. Feng [32] performed particle trajectory simulations for a tapered nozzle with particle size ranging from 0.5 μm to 3 μm and S/W ranging from 0.5 to 4. Feng's [32] simulations ignored particle bounce; particles were considered deposited as soon as the trajectory came to within one particle radius of the surface. These simulations agreed with the experimental results of Sethi & John [31] in that the particle surface density is minimum at the nozzle axis and peaks towards the nozzle edge. How radial profiles of particle concentration are affected by bounce has not been explored.

The experimental studies on particle bounce in impactors presented above present conclusions regarding particle bounce using the collection efficiencies obtained for different conditions [13,15,20,21,23] or by looking at the presence of secondary deposits or lack thereof [29,30]. The shortcoming of these approaches is that they fail to provide an understanding of the cause and underlying physics of particle bounce in impactors and how that bounce affects deposition pattern and overall collection efficiency.

A goal of the present work is to place the study of particle bounce, particle deposition, and the resulting deposition patterns on a firmer physical footing. We do this using extant models for particle impaction on flat plates [33,34] which use an energy balance between the particle kinetic energy and the surface adhesion energy due to van der Waals forces to derive a critical particle velocity necessary for a particle to bounce off a flat surface [35]. The adhesion energy between a particle of a certain diameter and a flat surface at a fixed separation distance is directly proportional to the Hamaker constant (A) which is a function of macroscopic properties of both the interacting particle and the surface [36,37]. The recovered kinetic energy of the particle is directly proportional to the square of the coefficient of restitution (e) which is the ratio of normal rebound particle velocity to the normal incident particle velocity. Thus, the critical velocity for the particle to bounce can be obtained from the difference between the recovered kinetic energy of the particle and the adhesion energy between the particle and the surface. Via this approach, knowledge of A and e, allows simulation of a particle trajectory, and prediction of whether bounce occurs or not, as well as a tracking of any subsequent trajectory to determine the ultimate fate of the particle.

Herein we hypothesize that with increase in relative humidity, particles adsorb water on their surface which decreases the adhesion energy between the particles and a hydrophobic surface thereby increasing the likelihood of bounce. We demonstrate that (as expected) this is indeed the case by conducting experiments of hygroscopic particles impacting a hydrophobic surface for a range of relative humidities. The change in particle deposition patterns with relative humidity is less straightforward. To explain it, we conduct particle trajectory simulations, iteratively varying (A,e) until the simulations agree with the experiments. We show that the simulations give qualitatively the same deposition patterns as the experiment and explain how the multibounce character of the particle trajectories causes the resulting deposition patterns.

2. Experimental method

Fig. 4 is a schematic of the experimental setup used. Monodisperse particles, generated using a vibrating orifice aerosol generator (VOAG - TSI Model 3450) were introduced into an airstream and passed through a circular nozzle to create a particle laden jet. The jet was then directed at a glass slide that served as the impaction plate. Disodium fluorescein (DSF) particles of diameter $d = 12.8$ μm were used in this work. DSF is a water-soluble fluorescent dye having a density $\rho_p = 1600$ kg/m^3 [38]. A DSF solution was made using a 25/75 (v/v) water/isopropyl alcohol solvent as opposed to the 50/50 (v/v) water/isopropyl alcohol solvent typically used [39] to have greater control over relative humidity; the lowered water content of the solvent reduced fluctuations of the relative humidity in the air flow. The DSF solution was pumped at a fixed flow rate of 30 ml/h into the VOAG using a syringe pump. The resulting monodisperse drops of DSF solution generated by the VOAG micro-orifice were flowed through a vertical drying column by dilution air. The dilution air consisted of house air having a relative humidity of 5%

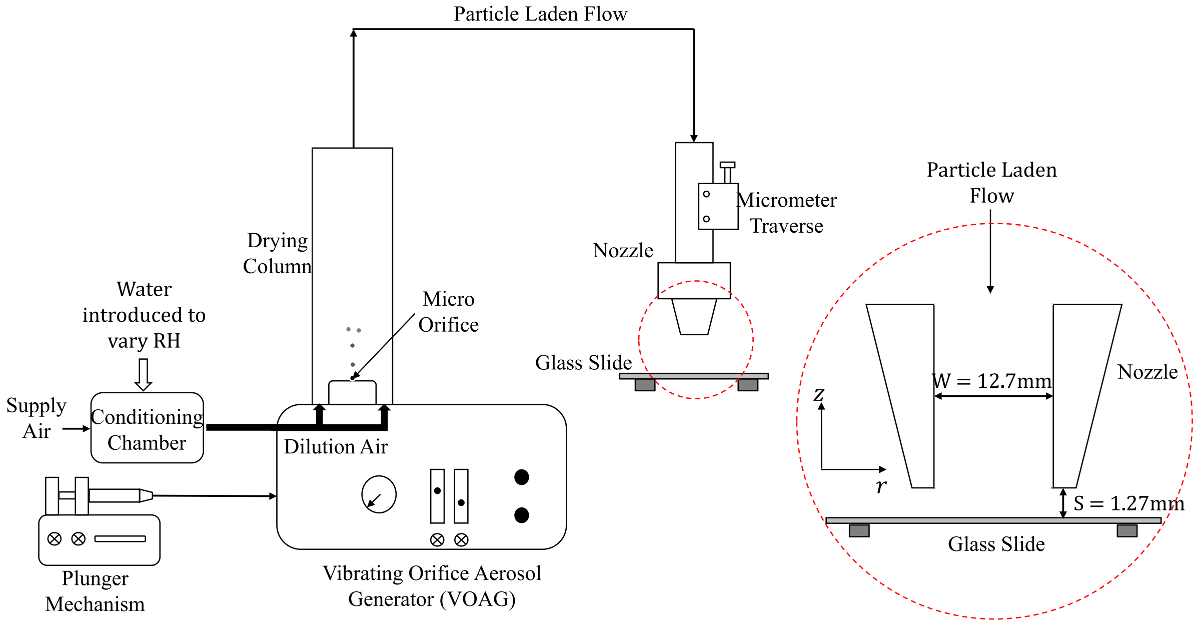

Fig. 4. Schematic of experimental setup. The part of the schematic which is circled in red is presented in the inset to show a more accurate representation of the S/W used. (For interpretation of the references to colour in this figure legend, the reader is referred to the web version of this article.)

leading to evaporation of the isopropyl alcohol and water and leaving behind a monodisperse distribution of DSF particles. Charging of the resulting particles was minimized by passing the dilution air through a Kr-85 neutralizer (TSI Model 3077A).

The particle diameter d was obtained from the equation:

$$d = C^{1/3} d_d \tag{2}$$

where d_d is the drop diameter and C is the concentration (v/v) of the DSF solution. The VOAG frequency necessary to generate the desired drop diameter was computed from:

$$d_d = \left(\frac{6Q}{\pi f}\right)^{1/3} \tag{3}$$

where f is the frequency of the orifice and Q is the liquid feed rate.

The dry monodisperse aerosol particles generated by the VOAG were carried by the dilution air through a nozzle consisting of three stages: an expansion plenum, a flow straightener, and the nozzle proper whose profile conformed to a fifth order polynomial, enabling generation of a uniform velocity profile at the nozzle exit according to the design of Bell & Mehta [40]. The nozzle inner profile decreased from a diameter of 43.2 mm at the inlet to 12.7 mm at the exit while moving 32 mm along the nozzle axis. Since the nozzle profile was continuously curved, the throat length was zero and nozzle angle variable. The jet/nozzle diameter was $W = 12.7$ mm, and the nozzle orifice was surrounded by a flat 5 mm flange which ran parallel to the impaction plate. The velocity at the nozzle exit was 8 m/s as measured by a TSI Velocicalc 9515 anemometer, giving $\sqrt{Stk} = 1.02$ and a jet Reynolds number $Re = 6920$. The nozzle was vertically mounted on a micrometer traverse to provide a downward facing jet oriented normal to the impaction plate having controllable S/W, which was set to 0.1 for the experiments presented herein. This S/W is similar to those used in previous studies where secondary deposits were observed [28,29]. The S/W value chosen here, though smaller than the normal operation $S/W \sim 1$ for most impactors, has shown to produce particle size dependent deposition patterns which have a potential to improve sub-stage resolution in inertial impactors [39,41].

The impaction plates were 4″ x 3″ glass slides coated with a film of petroleum jelly. The coating process consisted of dipping the slides in a solution of petroleum jelly dissolved in heptane in a 1:10 (v/v) petroleum jelly to heptane ratio. Upon extraction from the solution, excess solution was wicked from the edge of the slide and the slide was then placed flat under a fume hood for 30 min to dry. This process, originally due to Sethi & John [31], results in a uniform petroleum jelly coating. The glass slide was mounted on an optical lens holder which was fixed on an optics table and located directly beneath the nozzle. The aerosol impaction time for each run was 10 min which ensured significant particle deposition. The wettability of the petroleum jelly coated glass slide was quantified via the contact angle of water on the surface, which was 103° and therefore hydrophobic, as expected. The contact angle was measured by depositing a water drop on the coated glass slide and taking an image of the liquid/solid interface via a camera whose optical axis ran along the surface of the glass slide. The contact angle was measured from the image using the ImageJ software package.

A range of relative humidities for the nozzle flow was obtained via the following procedure. House air having a relative humidity of 5% was passed through a conditioning chamber (see Fig. 4) containing beakers filled with water at a temperature of 99 °C. The air exiting the conditioning chamber flowed into the VOAG to carry the DSF particles to the nozzle. At the beginning of each run, relative humidity measurements of the flow were made at the nozzle exit using an EXTECH EA 25 hygrometer. Once the measurements stabilized, the relative humidity was recorded, and the impaction plates placed under the nozzle to begin the experiment. The amount of water introduced in the conditioning chamber was increased to obtain higher relative humidities. Experiments were conducted for relative humidities ranging from 8% to 57%. Once particle impaction was concluded, the glass slides were removed and immediately imaged at 1× using a Canon Rebel T3i digital camera paired with a Canon EF-S 18-55 mm f/3.5–5.6 IS STM Lens. Another set of 1× images of the coated slides with no particle deposition were taken as reference. The 1× images of both the particle slides and the blank slides were then analyzed using an image processing routine written in the MATLAB programming environment. For both sets of images, the geometric center was identified, and then radial profiles were obtained via azimuthal averaging. The resulting radial profiles are referred to as I_p for the images of particle impaction and I_r for the reference or blank slides. The radial profiles presented here are the difference between the two:

$$I = I_p - I_r \quad (4)$$

We assume that I is proportional to the particle surface density, a reasonable assumption for monodisperse particles as long as no more than one layer of particles accumulates during the course of an experiment, which is the case here. Hence the images and plots presented in the next section are of number of particles/area.

3. Results

Sample images are presented in Fig. 5 of the particle deposition patterns for three relative humidities. Hereinafter we refer to relative humidity via the variable ϕ with a range [0,1]. The figure reveals a decrease in overall particle deposition with ϕ. The disks are the primary deposits and have a diameter close to that of the nozzle. The surrounding deposits readily visible in Fig. 5(a) and Fig. 5(b) (and present, but not visible in Fig. 5(c)) are the secondary deposits which are located beyond the nozzle edge and are sometimes referred to as halos in the literature. The visual results are quantified in Fig. 6 which is a plot of image intensity I in arbitrary units versus normalized radius r/R where R is the nozzle radius ($R = W/2 = 6.35$ mm) for $\phi = 0.08$–0.57, all the cases considered here. To reduce clutter and clearly reveal the variation in radial particle surface distribution with ϕ, a scaled intensity I_s (I scaled to the maximum value for the given ϕ) versus r/R plot is presented in *Fig. 7* where four representative values of ϕ are included. To facilitate observation of the effect of humidity, the results plotted in *Fig. 6* and Fig. 7 are arbitrarily partitioned into low ϕ (black) cases and high ϕ cases (blue), $\phi = 0.3$ separating the two. The marker size of the black lines increases with ϕ from 0 to 0.3. Separately, the marker size of the blue lines increases with ϕ from 0.3 to 0.57. A sample image of deposited DSF particles under a scanning electron microscope (SEM) is shown in *Fig. 8* to show the morphology of the deposited particles. The image shows that the deposited particles retain their shape and have sufficient inter particle distance which agrees with our assumption of mono layer particle deposition on the substrate.

The radial profiles presented in *Fig. 6* reveal a decrease in I with ϕ at virtually every radial location, demonstrating that, as expected, as the particles contain more moisture, fewer deposit on the hygroscopic surface used here. This is further quantified in Fig. 9 which is a plot of the area under each of the radial intensity plots presented in *Fig. 6*, E, versus ϕ. This area, E, is proportional to the number or particles collected and thus Fig. 9 shows that the collection efficiency decreases with ϕ for these hygroscopic particles on this hydrophobic surface. It is assumed that all particles generated by the VOAG exit the nozzle and thus the same number of particles exited the nozzle for all the experiments conducted.

In every plot shown in Fig. 6 we see an increase in particle surface density with radius when moving from the nozzle axis to just inside the nozzle edge, where the peak density occurs. The particle surface density then falls steeply with radius before increasing again outside the nozzle edge, forming a second peak. To clearly distinguish the secondary

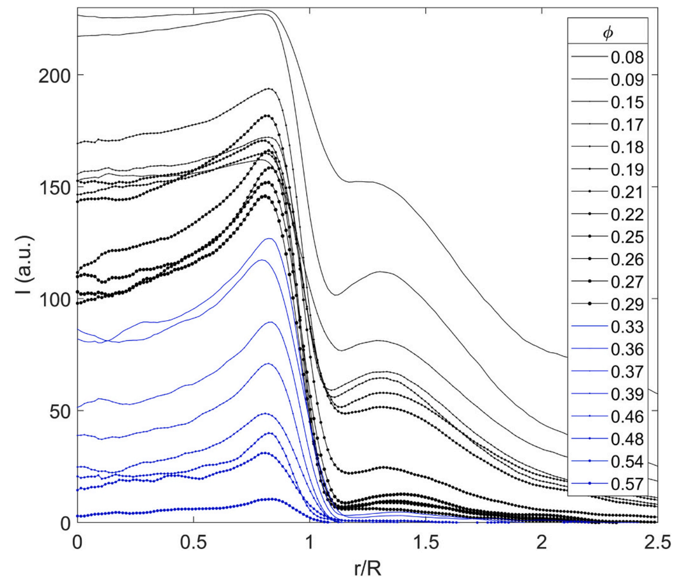

Fig. 6. Intensity I versus normalized radial location, r/R for all ϕ explored in these experiments. The black lines denote low ϕ cases ($\phi < 0.3$). The marker size of the black lines increases as ϕ increases from 0 to 0.3. The blue lines denote high ϕ cases ($\phi > 0.3$). The marker size of the blue lines increases as ϕ increases from 0.3 to 0.57. (For interpretation of the references to colour in this figure legend, the reader is referred to the web version of this article.)

deposit from the primary deposit, we classify any particle deposit within the nozzle edge, i.e., $r/R < 1$ as the primary deposit while any particle deposition beyond the nozzle edge, i.e., $r/R > 1$ as the secondary deposit. Particle collection in both the primary and secondary region decreases with ϕ, though more so for the secondary deposits than the primary. Fig. 7 shows that the maximum particle surface density occurs near the nozzle edge $r/R \sim 1$, and at essentially the same radial location for all ϕ.

The two peaks, one just inside the nozzle edge, i.e. $r/R < 1$, and the other outside the nozzle edge, $r/R > 1$ are referred to as the primary and secondary peaks, r_1 and r_2, respectively, and made dimensionless as $R_1 = r_1/R$ and $R_2 = r_2/R$. These are plotted against ϕ in Fig. 10, showing very little variation in these peak locations with relative humidity, except for a small decrease in the secondary peak location at the highest relative humidities.

4. Discussion

The first goal of this research was relatively straightforward: to demonstrate, through particle impaction experiments, that adhesion of hygroscopic particles with a hydrophobic surface will decrease with

(a) (b) (c)

Fig. 5. Sample images of the deposition pattern for relative humidity ϕ of (a) 0.09, (b) 0.22, and (c) 0.57.

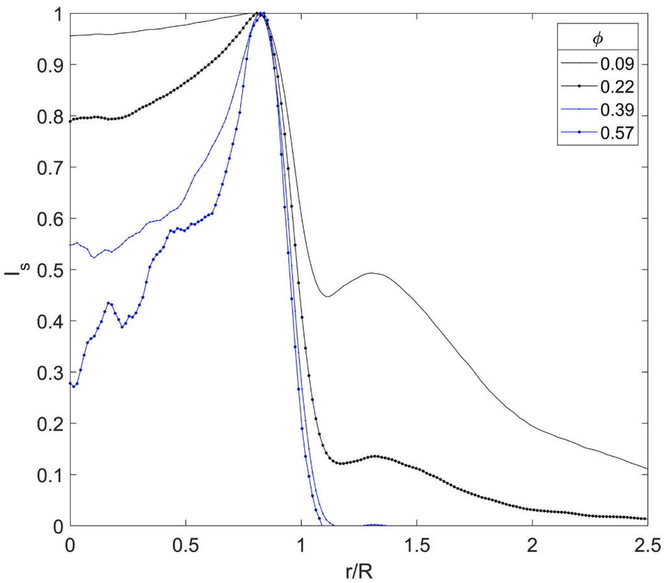

Fig. 7. Scaled intensity I_s versus r/R for ϕ of 0.09, 0.22, 0.39 and 0.57. The black lines denote low ϕ ($\phi < 0.3$) and the blue lines denote high ϕ ($\phi > 0.3$). The marker size of the black lines increases as ϕ increases from 0 to 0.3. The marker size of the blue lines increases as ϕ increases from 0.3 to 0.57. (For interpretation of the references to colour in this figure legend, the reader is referred to the web version of this article.)

relative humidity, thereby leading to a decrease in particle collection. As shown qualitatively in Fig. 5 and in Fig. 9, the number of particles collected on the petroleum jelly coated substrate decreases with ϕ, showing that this is indeed the case.

The second goal of this research was more challenging, namely, to explain the change in particle deposition pattern, specifically the formation of secondary deposits and the change in these deposits that occurs with changes in ϕ. The experiments presented here reveal this change in deposition pattern and can be observed in Fig. 5 through *Fig.* 7. However, the mechanism responsible for these patterns in terms of bounce or the lack thereof cannot be elucidated from the experimental results given our inability to actually visualize the particle impact phenomena. Indeed, even the reduction in particle deposition with ϕ cannot be explained in terms of any effect that particle bounce might have on this observation for this same reason. Accordingly, here we resort to particle trajectory simulations to determine if particle bounce occurs, to what degree it occurs, and if/how it may explain the secondary deposits that are observed. These trajectories are based on a model for particle bounce tailored to the experimental conditions used in this research.

For these simulations, the flow field was first computed in Fluent assuming axisymmetry and using the exact dimensions of the nozzle employed in the experiments, including the internal contours and the

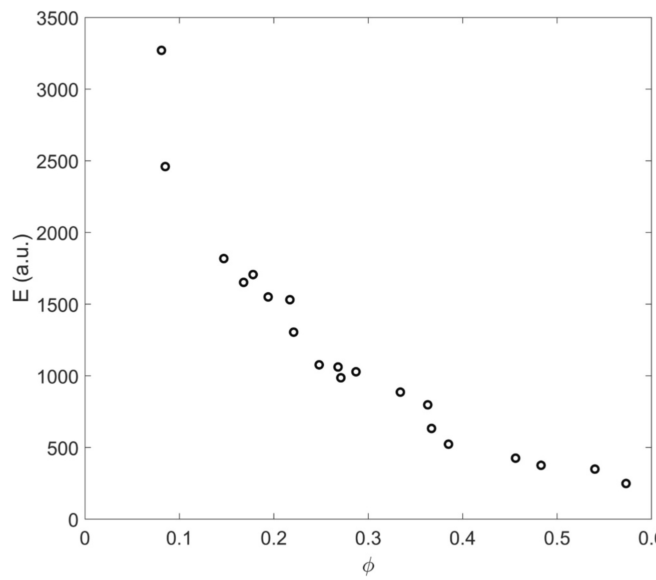

Fig. 9. Area under intensity plots E versus relative humidity ϕ.

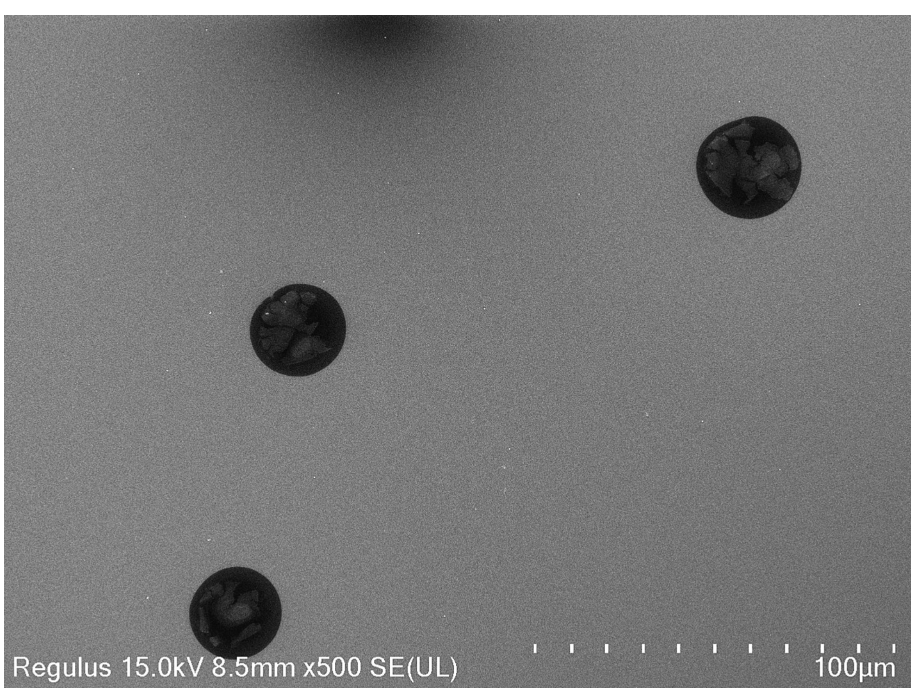

Fig. 8. A sample image of deposited disodium fluorescein (DSF) particles for $\phi = 0.09$ case under a scanning electron microscope (SEM). The image is captured at 500× zoom using a HITACH Regulus 8250 SEM.

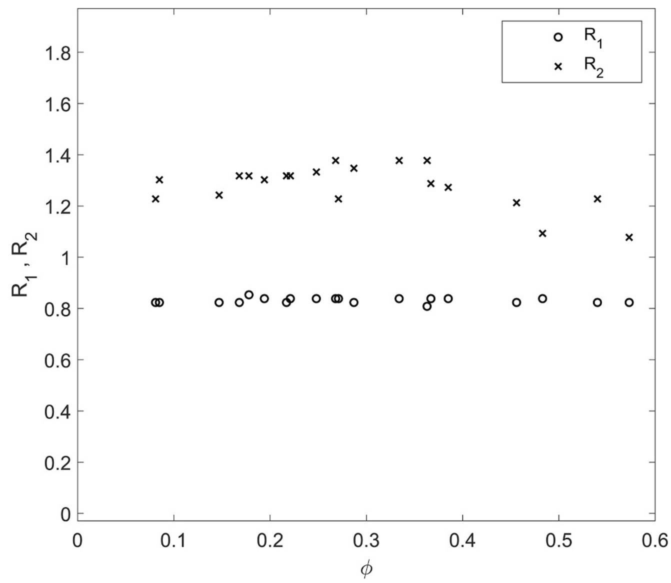

Fig. 10. Dimensionless primary peak radial location, R_1 and secondary peak radial location, R_2 normalized to the nozzle radius versus ϕ.

external structure, i.e. the flat flange on the face and the angle of the external face of the nozzle outside of the flange area (See Fig. 4). A multizone quadrilateral and triangular mesh was used. The mesh elements were ~ 1 μm in size along the impaction plate and increased axially as the nozzle inlet was approached. No mesh element was larger than 30 μm. The inlet plane was set as 'velocity inlet' with 0.68 m/s axial velocity and no radial velocity, the oultlet plane was set as 'outflow', the impaction plate and the nozzle contour were set as 'wall' and the nozzle axis was set as 'axis'. A steady state pressure based solver along with viscous-laminar model was employed to compute the flow field. Once the flow field was computed, trajectories were obtained for particles having the same diameter as those used in the experiments. These trajectories began at the nozzle inlet. The force acting on each particle is $F = F_d + F_g$, where F_d is the drag force, and F_g is the gravitational force where:

$$F_d = \frac{3\pi\mu V_r d}{C_c} \tag{5}$$

where μ is the absolute viscosity of air, $V_r = V - V_p$, the particle velocity relative to the local flow velocity, and C_c is the Cunningham correction factor which should be assumed for particle <10 μm for accuracy [35]:

$$C_c = 1 + \frac{\lambda}{d}\left[2.51 + 0.80exp\left(-0.55\frac{d}{\lambda}\right)\right] \tag{6}$$

where λ is the mean free path of air. The gravitational force is:

$$F_g = mg \tag{7}$$

where m is the particle mass and g is the gravitational acceleration. The particle velocity was updated at each time step by integrating:

$$m\frac{dV_p}{dt} = F_d + F_g \tag{8}$$

to give:

$$V_p(i+1) = V_p(i) + \frac{(F_d + F_g)(\Delta t)}{m} \tag{9}$$

A time step $\Delta t = 10^{-6}$ s was used. For all simulations, the jet flow rate and S/W was the same as for the experiments.

Once the particle center is within one half diameter of the impactor plate, it can either stop and deposit or bounce based on its interaction with the surface and its incident velocity. The criterion for particle bounce was based on the energy balance model for a particle impacting a solid surface given by Dahneke [33] which states that particle rebound occurs when the recovered normal direction kinetic energy of the particle at contact is greater than the adhesion energy of the surface. The model assumes that: (i) the tangential kinetic energy of the particle is conserved, (ii) the particles are perfectly smooth, solid, and non-rotating spheres, and (iii) the impacted surface is perfectly smooth and solid. The resulting energy balance is:

$$E_{k,n,r} = e^2 E_{k,n,i} - \left(1 - e^2\right)E_a \tag{10}$$

where $E_{k,n,r}$ is the normal direction rebound kinetic energy of the particle, $E_{k,n,i}$ is the normal direction incident kinetic energy of the particle, E_a is the adhesion energy of the surface, and e is the coeficient of restitution which is the ratio of normal rebound velocity of the particle ($v_{n,r}$) to the normal incident velocity of the particle ($v_{n,i}$). The adhesion energy is expressed as [36,42,43]:

$$E_a = \frac{Ad}{12z_0} \tag{11}$$

where A is the Hamaker constant and z_0 is the equilibrium separation distance of two spheres assumed to be 0.2 nm (Israelachvili **Error! Reference source not found.Error! Reference source not found.**1992). Combining Eqs. (10) and (11) gives:

$$E_{k,n,r} = e^2\frac{1}{2}m{v_{n,i}}^2 - \left(1 - e^2\right)\frac{Ad}{12z_0} \tag{12}$$

The limiting condition for particle bounce is obtained by setting $E_{k,n,r}$ in Eq. (12) to zero, giving the critical velocity v_c, which is the normal incident velocity of the particle above which particle bounce occurs and below which particle deposition occurs:

$$v_c = \left(\frac{(1 - e^2)Ad}{6mz_0e^2}\right)^{1/2} \tag{13}$$

For fixed values of A and e, a critical normal velocity is obtained at each impact location which is compared to the particle normal velocity. Deposition occurs if the particle normal velocity is less than v_c, and the simulation for that particular particle is terminated. If the particle normal velocity exceeds v_c, the particle rebounds with a normal velocity equal to:

$$v_{n,r} = \left(e^2 - \left(1 - e^2\right)\frac{Ad}{6z_0m{v_{n,i}}^2}\right)^{1/2} v_{n,i} \tag{14}$$

This resulting rebound velocity (using the conserved tangential velocity to complete this vector) is used in Eq. (9) and computation of the particle trajectory is continued. At each intersection of particle trajectory with the impaction surface, a check for bounce is performed until the particle either deposits or exits the domain. Once all the deposition locations are obtained, they are binned and a scaled surface density $N_s = N/N_m$ versus r/R plot is obtained, where N is the number of particles per unit area on the impaction surface and N_m is the maximum particle surface density for a given ϕ. Scaled in this way, these plots can be compared to the scaled experimental plots shown in Fig. 7. Out of the twenty relative humidities explored in the experiments, six were chosen for simulation: $\phi = 0.09$, 0.17, 0.22, 0.29, 0.39, and 0.57.

For the disodium fluorescein particles and petroleum jelly covered surface considered here, values of A and e were unavailable. These values were obtained by iteratively varying (A, e) until the resulting plot of N_s versus r/R agreed with the experimental I_s versus r/R plot for each of these six ϕ. This search for (A, e) began by exploring the parameter space for A ranging from $1 \times 10^{-21}J$ to $1 \times 10^{-15}J$ while e ranged from 0 to 1. The typical range of A for inorganic salts is $1 \times 10^{-21}J$ to $1 \times 10^{-19}J$ [44] but a wider range is explored in these simulations to ensure that an accurate value for A is obtained. For each (A, e) 2151 particle trajectories were simulated. The trajectory starting points were placed at equal separation of 0.01 mm from each other at the nozzle inlet starting at $r = 0.1$ mm and moving radially outward towards the nozzle wall. At each (A, e) an N_s versus r/R plot was obtained, and four characteristics were obtained: primary peak location (R_1), secondary peak location (R_2), center height (S_0) and secondary peak height (S_2). These were compared to the corresponding values of the experimental intensity plots for the six ϕ explored as shown in Fig. 11. The degree of agreement between the simulation and experiment for each (A,e) was quantified by taking the sum of the square of the differences of the four characteristic values:

$$S = (R_1 - R_{1,s})^2 + (R_2 - R_{2,s})^2 + (S_0 - S_{0,s})^2 + (S_2 - S_{2,s})^2 \tag{15}$$

Where the subscript "s" denotes the value for the simulation.

Once all S values were computed for a broad (A,e) matrix a surface plot of A, e, S was plotted and the minima identified as shown in Fig. 12. Fig. 12 shows a surface plot for the broad A, e matrix for the $\phi = 0.09$ case. The process was then repeated for an (A, e) region around the minimum and with smaller increments of A and e, specifically $1 \times 10^{-20} J$ for A, and 0.001 for e. Following the process for computingting S for the smallest increments of A and e, $1 \times 10^{-20} J$ and 0.001 respectively, the value of (A,e) at the minimum S was taken as the actual (A,e) for that ϕ. Confidence that the minimum in S is global is obtained from the very large range of A explored and that the complete range of possible e is explored.

The resulting (A, e) are presented in Table 1 which shows that A decreases with ϕ which is expected because A is the measure of attraction of particle to the surface, and the surface is hydrophobic. On the other hand, e is essentially constant for $\phi = 0.09$ to 0.29 but increases with ϕ from 0.29 to 0.57. This can be explained by the particle formation characteristics. When generating solid particles using a VOAG, perfectly spherical particles are usually obtained by using a solution of the solute with 50/50 (v/v) water/isopropyl alcohol solvent [45]. As noted earlier, a 25/75 (v/v) water/isopropyl alcohol solvent was used in the current experiments; the lower water content reduced fluctuations of ϕ in the flow. However, the greater alcohol content in the solution speeds the drying of the drop generated by the aerosol generator causing the formation of solid at the surface before the core is fully evaporated. When the core finally evaporates, the cell collapses or shrinks forming asperities on the particle surface [46]. It is known that e decreases with surface roughness due to plastic deformation of the asperities of the particle during particle impaction [47–50]. At low ϕ, this effect is maximized since the evaporation rate will be greatest, explaining the low value of e in Table 1 at low ϕ as well as the rise in e at high ϕ.

The resulting scaled particle surface density radial profiles for $\phi = 0.09$, 0.22, 0.39 and 0.57 are presented in Figs. 13, 14, 15 and 16 along

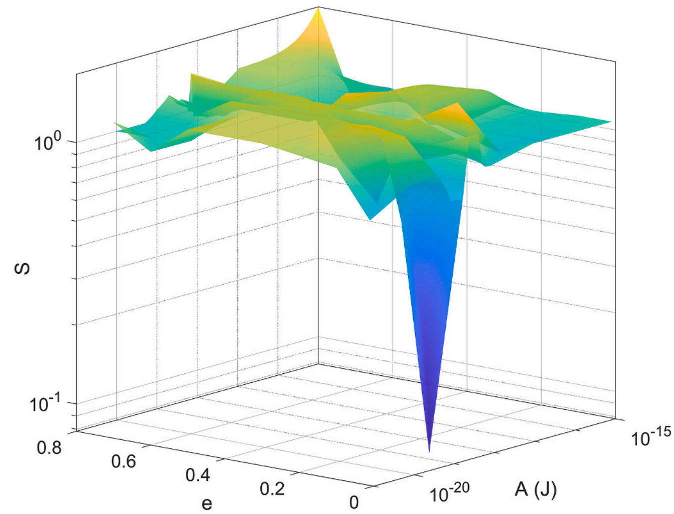

Fig. 12. Surface plot of S versus (A, e) for $\phi = 0.09$. Broad case.

Table 1
Hamaker constant A, coefficient of restitution e, and the critical velocity for bounce v_c for the six ϕ values considered in the energy analysis.

ϕ	A (J)	e	v_c (m/s)
0.09	2.6×10^{-19}	0.11	0.36
0.17	2.4×10^{-19}	0.11	0.34
0.22	1×10^{-19}	0.10	0.25
0.29	6×10^{-20}	0.09	0.21
0.39	4×10^{-20}	0.14	0.11
0.57	1×10^{-20}	0.31	0.02

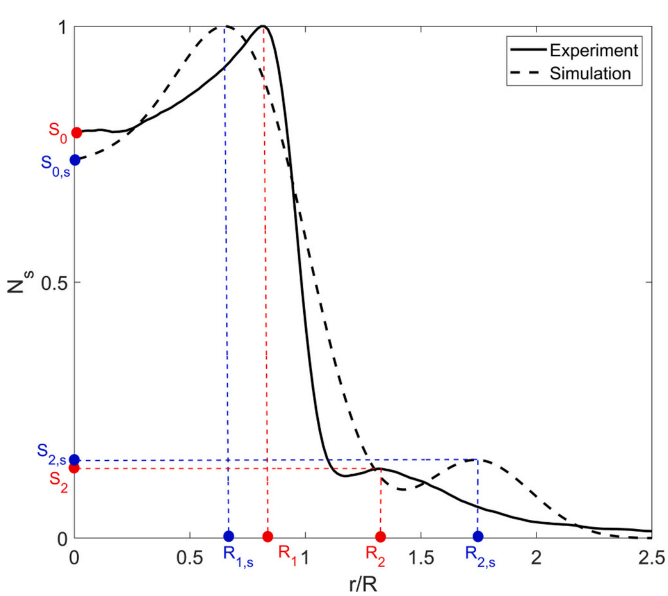

Fig. 11. Plot of N_s versus r/R comparing the experiment and simulation using four characteristics: primary peak location (R_1), secondary peak location (R_2), center height (S_0) and secondary peak height (S_2). The subscript "s" refers to the simulations.

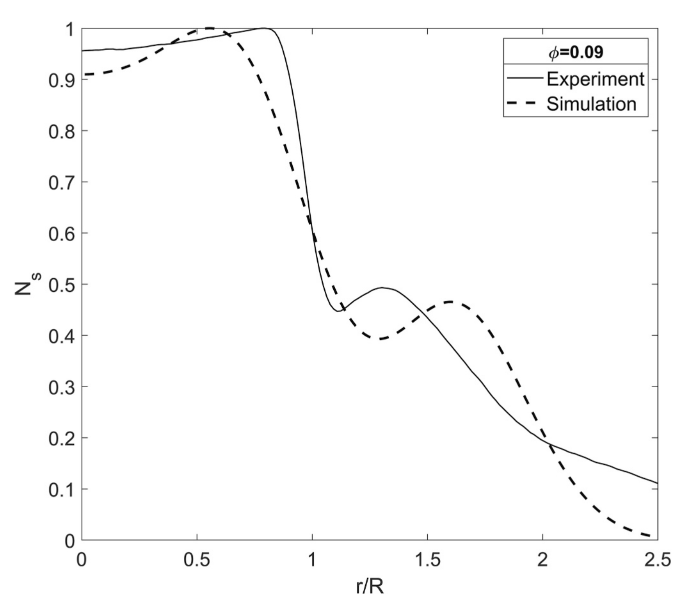

Fig. 13. Plot of N_s versus r/R for $\phi = 0.09$. The solid black line is the experimental scaled particle surface density plot. The dashed black line is the scaled particle surface density obtained from the simulations.

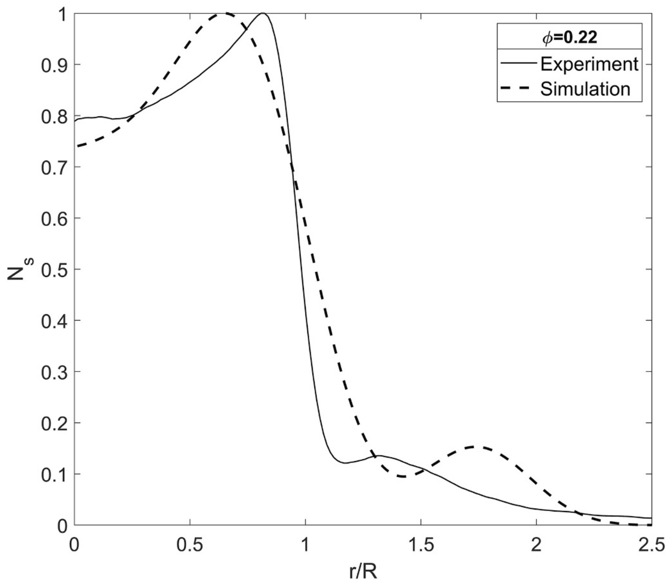

Fig. 14. Plot of N_s vs r/R for $\phi = 0.22$. The solid black line is the experimental scaled particle surface density. The dashed black line is the scaled particle surface density obtained from the simulations.

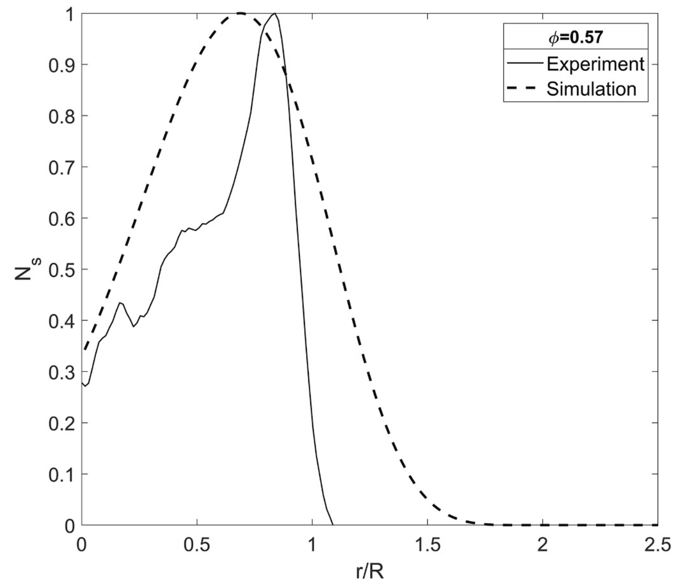

Fig. 16. Plot of N_s versus r/R for $\phi = 0.57$. The solid black line is the experimental scaled particle surface density. The dashed black line is the scaled particle surface density obtained from the simulations.

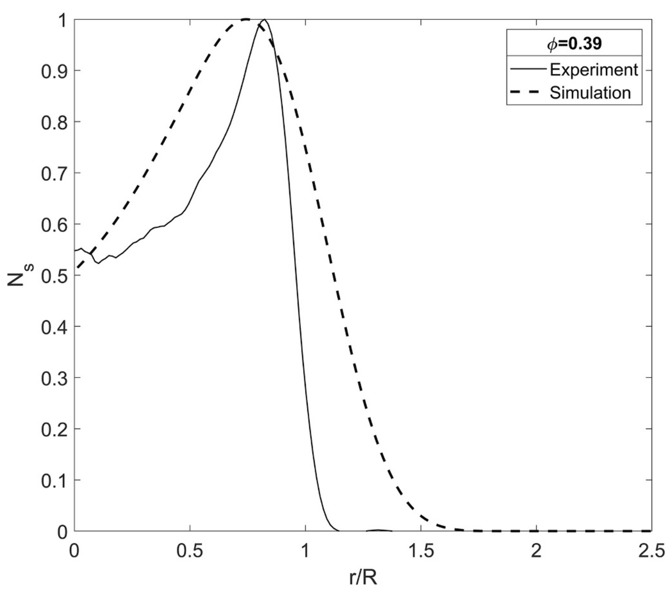

Fig. 15. Plot of N_s vs r/R for $\phi = 0.39$. The solid black line is the experimental scaled particle surface density. The dashed black line is the scaled particle surface density obtained from the simulations.

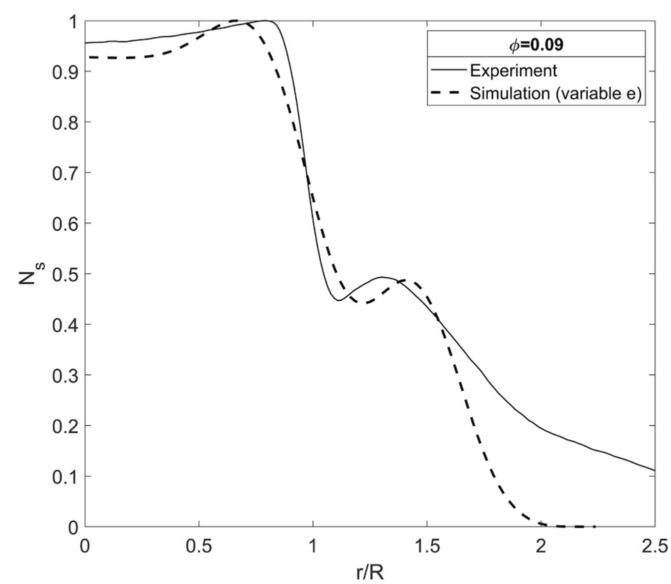

Fig. 17. Plot of N_s versus r/R for $\phi = 0.09$ using a variable e for the simulations. The solid black line is the experimental scaled particle surface density plot. The dashed black line is the scaled particle surface density obtained from the simulations.

with their experimental counterparts. These four were chosen from the six presented in Table 1 as representative of the range explored. These figures show that the scaled particle surface densities agree with the experimental results reasonably well, though not perfectly. Part of the reason for the differences is likely due to the constant value of e which was considered for the simulation for a given ϕ. The literature suggests that e can be a function of the angle of incidence of impact [51,52] which are not constant for all trajectories considered in the simulations used in this paper. A sample case where e varies with angle of incidence (Tabhoff and Malak,1987) and A is held constant at $2.6 \times 10^{-19} J$ was performed for the $\phi = 0.09$ case, is shown in Fig. 17. Note here that the angle of incidence refers to the angle made by the particle trajectory with the impaction surface. The e versus angle of incidence function used in Fig. 17 was obtained by curve fitting normalized e versus angle of incidence data from Tabhoff and Malak [53] for 15 μm fly ash particles targeting steel plates. The normalized curve fit function was then multiplied by the value of e obtained from our simulation for $\phi = 0.09$ (e=0.11) to obtain the e versus angle of incidence function. It is noted that by incorporating variation of e with angle of incidence in Fig. 17, the peaks $R_{1,s}$ and $R_{2,s}$ are closer to their experimental counterparts, compared to Fig. 13. This notwithstanding, we did not incorporate this functionality herein because we do not have information on the actual functional form that should hold for our fluorescein/petroleum jelly system.

Even with a fixed e the simulations reveal the same trends as in the experiments, namely greater particle surface density near the nozzle edge than at the nozzle axis for the primary deposit for all ϕ and a decrease in the particle surface density at the center with increasing ϕ. The simulations also replicate the decrease in particle surface density of secondary deposits as ϕ increases from 0.09 to 0.57. The location of the peak surface density in the primary and secondary deposits is imperfectly predicted by the simulations, again, probably due to deviations of the assumptions from the actual case.

Fig. 18 is a plot of N (the unscaled surface density) versus r/R obtained from the particle trajectory simulations for $\phi = 0.09$, 0.22, 0.39, and 0.57 showing that the overall particle collection decreases with ϕ. This agrees qualitatively with the experimental results where E, the area under the intensity plots, decreases with ϕ, as shown in Fig. 9.

We now use the particle trajectories obtained in the simulations to explain the salient features of the experimental results. Specifically, we explain (i) why there is a primary and a secondary peak, (ii) why both peaks decrease with increasing ϕ (Fig. 6), (iii) why the radial location of both peaks is essentially a constant, independent of ϕ, and (iv) why the secondary peak decreases with ϕ more rapidly than the primary peak (Fig. 7). This last point is especially important, since it concerns, at least with regard to variable relative humidity, why secondary patterns (i.e., halos) are sometimes present and sometimes absent.

The primary peak observed in the experiments and simulations can be thought of as a reduction in spacing between deposit locations at the impaction surface near r/R=1 compared to other radial locations, of the trajectories that start out uniformly spaced at the nozzle inlet. The ultimate cause of this reduction in spacing can be traced to an increase in z-direction fluid velocity with r under the nozzle, combined with what happens to particles after they bounce. Fig. 19 is a plot of the z-direction fluid velocity $-v_z$ versus axial location z for 10 different radial locations r/R=0.1, 0.2, 0.3, 0.4, 0.5, 0.6, 0.7, 0.8, 0.9 and 1 showing that, for all z, $-v_z$ increases with r until just before r/R=1. Hence, as particle trajectories move radially outward, there is a growing downward flow velocity that acts to force particle trajectories downward, a tendency that peaks just before $r/R\sim1$. Of course, this only suggests that trajectories are more likely to impact the plate at larger r/R, but does not speak to whether those particle impacts will result in a deposition event. So, in combination with the z-direction velocity, we must now also consider bounce.

Fig. 20 reveals how both bounce and the characteristsics of the z-direction component of velocity combine to create the primary peak.

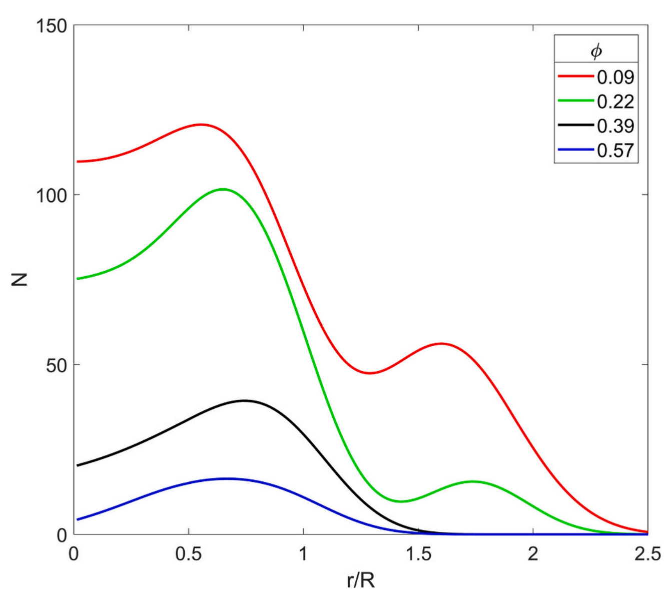

Fig. 18. Plot of N versus r/R obtained from the particle trajectory simulations for $\phi = 0.09$, 0.22, 0.39, and 0.57 showing that the overall particle collection decreases with ϕ. Specifically, out of 2151 particle trajectories, 1223 deposited for $\phi = 0.09$, 1019 for $\phi = 0.22$, 690 $\phi = 0.39$ for and 330 for $\phi = 0.57$.

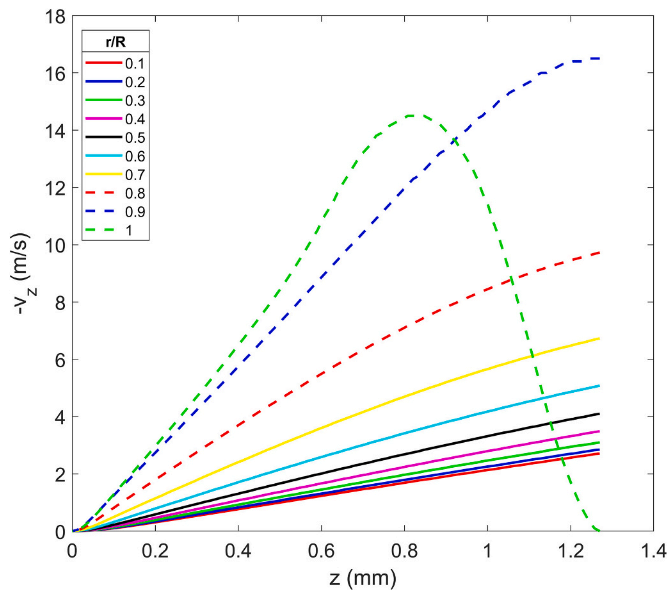

Fig. 19. Axial flow velocity -v_z versus axial location z under the nozzle (z = 0 to1.27 mm) for 10 different radial locations $r/R = 0.1$, 0.2, 0.3, 0.4, 0.5, 0.6, 0.7, 0.8, 0.9 and 1.

This figure presents particle trajectories for starting locations at the nozzle inlet ranging from close to the nozzle axis out to near the periphery. Note that only trajectories starting relatively close to the axis are presented in Fig. 20 to focus on the primary peak. The figure shows that particle deposition near the primary peak is due to particle trajectories that begin close to the axis, that bounce, and that then deposit some radial distance outward. The post-bounce radial distance that these particles travel decreases with the starting radial location. This is seen in the reduction with r in the separation of the deposition locations (the reduction in the distance between the blue dots) in Fig. 20. This reduction in the radial distance between deposition locations with r is caused by, as Fig. 19 shows, the increase in downward velocity with r. Stated another way, particles that start out at progressively larger radial locations will travel a shorter post-bounce radial distance because they are more effectively forced downward by the z-direction velocity. The reduction in separation between deposition locations manifests itself as a peak in particle number density at locations near $r/R\sim1$. This is less readily seen in Fig. 20(a) where ϕ is small. But this too agrees with both the experiments and simulations which show a peak near the nozzle periphery for small ϕ, but a peak that differs only a little from the particle concentration towards the nozzle center. In contrast, as shown in Fig. 20(d), the change in separation distance is more obvious at high ϕ, which again agrees with the experimental results and simulations which show a primary peak whose intensity is significantly different from that found towards the center when the humidity is high.

The above explanation necessitates a discussion of why, in the first place, all of the particle trajectories that result in deposition at or near the primary peak first bounce without depositing, as well as why at their subsequent impacts they stick. This is an important point because particles will bounce when their downward velocity exceeds the critical velocity (Eq. (13)). Hence, one might incorrectly presume that the large downward velocity that the trajectories experience after their first bounce would cause the particles to bounce yet again. The key to understanding this is to note that particle trajectories prior to their first bounce, impact the surface at close to normal incidence. Thus, their z-direction velocity is greater than critical and they bounce. However, after the impact and bounce, some of the kinetic energy of these particles is lost. Moreover, though these trajectories are now moving into a region with progressively higher downward velocity, it must be noted that the direction of the trajectory must first be reversed from its intially upward

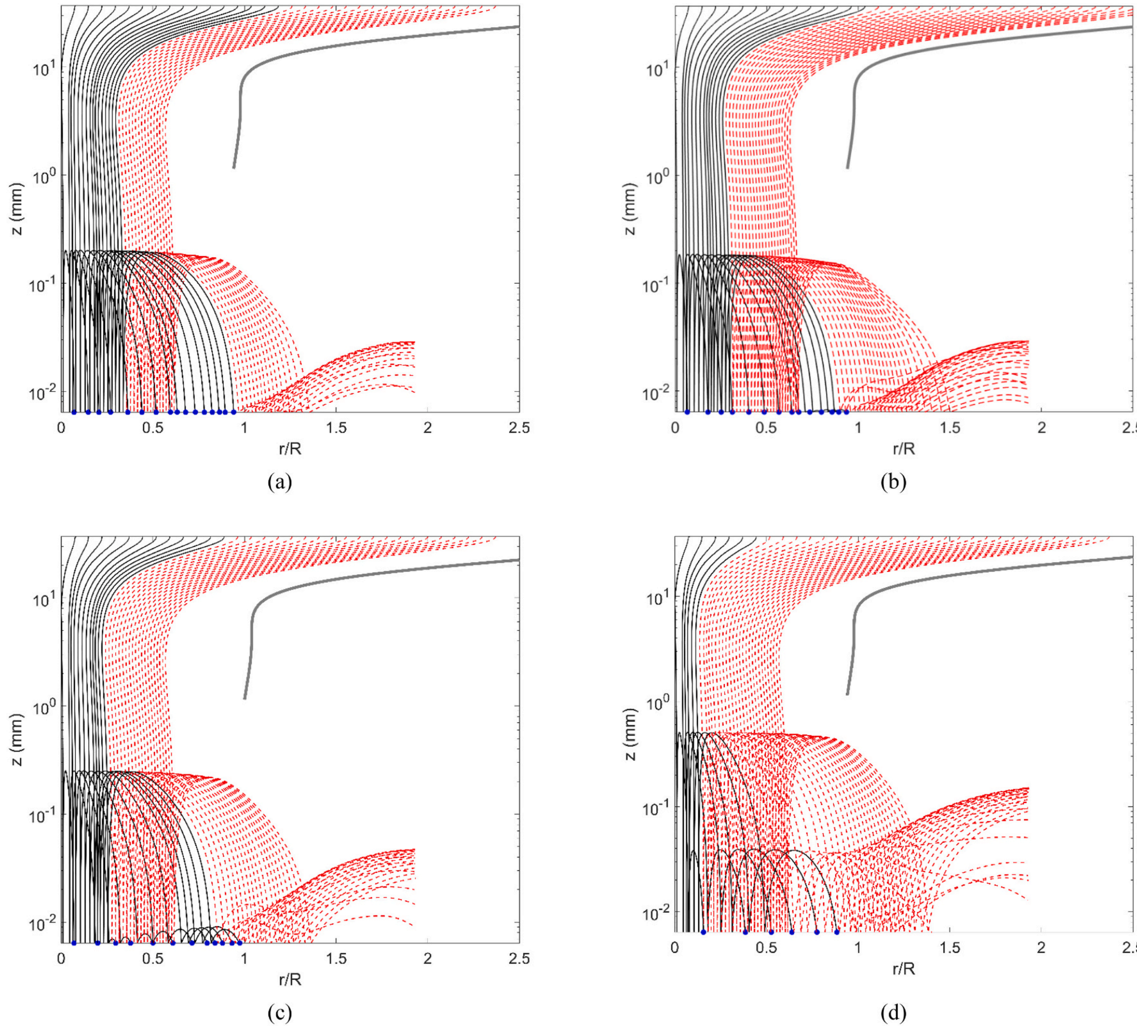

Fig. 20. Particle trajectories for: (a) $\phi = 0.09$, (b) $\phi = 0.22$, (c) $\phi = 0.39$, and (d) $\phi = 0.57$. For all (a), (b), (c) and (d), 32 trajectories are shown which start at equal separation of 0.5 mm from each other at the nozzle inlet starting at r=0.5 mm and moving radially outward. The trajectories in black (solid) are the ones which deposit while the trajectories in red (dashed) are the ones which fail to deposit. The y-axis is logarithmic to more clearly show the trajectories during particle bounce. The thick gray line is the nozzle inner surface; The blue dots represent the final particle deposition locations for the trajectories that deposit. (For interpretation of the references to colour in this figure legend, the reader is referred to the web version of this article.)

direction, before it can be accelerated back downward. Finally, at its second or third impact, where depostion occurs, the angle of incidence is farther from normal incidence, resulting in a lower z-direction impact velocity. These three effects reduce the z-direction velocity so that deposition can occur.

The primary peaks observed in both simulations and experiments are asymmetrical; on the right side of the primary peak, the intensity drops off dramatically and far less on the left. The reason for this is that, as shown in Fig. 20, there is a band of non depositing trajectories (red) with starting radial locations larger than those which result in deposition (black). These red trajectories result in particle bounce at their first impact, for the same reasons as the black trajectories. However, as they rise upward and move radially outward, they enter a region of (r, z) space where the z-direction velocity is quite large, as shown in Fig. 19, far larger than is the case for their black counterparts. Hence, in this case, though again the velocity field must first reverse the upward direction of the particle, the acceleration of the particle downward, once it does change direction is sufficiently large that it exceeds the critical velocity, and the particle bounces again, after which it travels out of the domain. This results in virtually no deposition at all just to the right of the peak near r/R=1 making the particle surface density on the right hand side of the primary peak drop precipitously with r, as is seen in the experiments and simulations. The same behavior is observed for high ϕ cases as well wherein the innermost trajectories form the primary peak and are then followed by a band of non-depositing trajectories.

Careful observation of the low ϕ ($\phi = 0.09$ to 0.29) and high ϕ ($\phi =$ 0.29 to 0.57) cases presented in Fig. 20*(a)* and *(b)* and Fig. 20*(c)* and *(d)*, respectively shows that, though the physics that cause the primary peak are the same, the behavior is slightly different. Specifically, for the high ϕ cases, the rebound of particle trajectories after bounce is higher, achieving a maximum height higher than that for the low ϕ cases. This is as expected. As noted above, e increases with ϕ for $\phi > 0.3$ which means the upward velocity after a bounce will be higher in (c) and (d) than in (a), as is the case. Also, for the black trajectories in Fig. 20*(c)* and *(d)*, the particles bounce twice before depositing. However, both the first and second bounce occur at a radial location less than the radial location of the second bounce for the red trajectories. Hence, the physics are the same. In other words, for the inner (black) trajectories, the downward fluid velocity is lower because it increases with r, while for the outer (red) trajectories, the downward fluid velocity is larger, sufficient to accelerate the particle to a velocity greater than critical and causing the particle to keep bouncing until it leaves the domain.

The secondary peak observed in the simulations and experiments is due to the same physics that produce the primary peak and can be best understood by reference to Fig. 21. This figure presents trajectories whose starting points begin at radial locations that begin where the starting points of those trajectories presented in Fig. 20 left off for $\phi = 0.09$ and 0.22. As Fig. 21 shows, these trajectories begin as red trajectories, trajectories that bounce twice, do not deposit, and leave the domain for the same reason as the red trajectories in Fig. 20. For these red trajectories, the first bounce is simply due to the z-direction particle velocity being larger than critical due to the close to normal incidence angle, while the second is due to the fact that the particle is exposed to an (r, z) location where the downward fluid velocity is quite high; in particular, the post-bounce trajectories reach their apex at r/R from 0.5 to 0.9 where the z-direction velocity is particularly large. This explains the large impact velocity and the second bounce. Now, as the starting location continues to move radially outward, close to the very edge of the nozzle inlet, the peak location of the post-bounce trajectory enters a region of r/R that ranges from slightly less than one to slightly greater than one. As shown in Fig. 22, in this region, the z-direction velocity drops significantly when compared to radial locations just inboard of this region. This results in a lower z-direction impact velocity for the particle, one that is lower than the critical velocity, resulting in deposition. This deposition occurs outside of the nozzle periphery i.e. $r/R>1$ due to the larger radial starting location. Comparing the $\phi = 0.22$ case to the $\phi = 0.09$ case in Fig. 21, since the critical velocity is lower for high ϕ than low ϕ, more trajectories bounce twice and leave the system for high ϕ, resulting in fewer secondary deposits. No plots are presented in Fig. 21 for $\phi = 0.39$ and $\phi = 0.57$ because no secondary deposits occur for these cases, in agreement with the experiments (see Fig. 15 and *Fig. 16*). This is because the coefficient of restitution for $\phi = 0.39$ and $\phi = 0.57$ are higher than for $\phi = 0.09$ and $\phi = 0.22$ and the critical velocity lower than for $\phi = 0.09$ and $\phi = 0.22$. Consequently trajectories starting at outer radial locations which impact outside of the nozzle periphery i.e. $r/R>1$ impact at high incident velocity and bounce again, thereby leaving the domain.

Next, we explain the decrease in both the primary and secondary peaks with ϕ. This decrease manifests itself in the plots presented in Fig. 20 as a reduction in the number of black trajectories as ϕ increases from (a) to (d), and similarly from (a) to (b) in Fig. 21. In all of these plots, the spacing in starting locations is identical, and hence fewer black trajectories imply fewer particles depositing at the relevant peak location (the primary peak for Fig. 20 and the secondary peak for Fig. 21). The cause for this is the fact that two things change as ϕ increases. First,

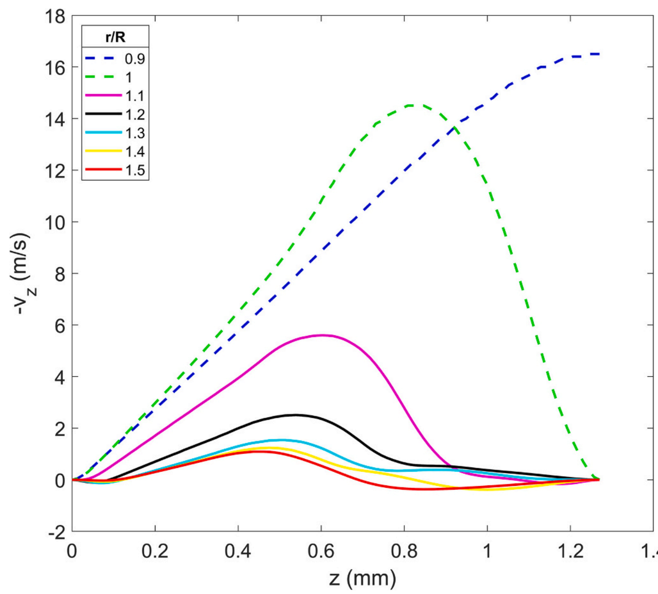

Fig. 22. Axial flow velocity $-v_z$ versus axial location z under the nozzle z=0 to z=1.27 mm for 7 different radial locations r/R=0.9, 1, 1.1, 1.2, 1.3, 1.4 and 1.5.

the critical velocity decreases. This can be seen in Eq. (13) which shows that the critical velocity v_c scales with A/e^2, which despite the squaring of e, is actually dominated by A here, due to the very large change in the Hamaker constant with humidity compared to the smaller change in e, as shown earlier. So, as ϕ increases, A drops and with it v_c as shown in Table 1. The decrease in v_c with ϕ causes fewer trajectories to deposit as primary and secondary deposits.

Secondly, for the higher ϕ region, e increases with ϕ. As noted above, this does not significantly affect v_c. But the increase in e with ϕ results in a higher apex in the particle trajectory after bounce for high ϕ than low ϕ. For the case of the primary peak, we refer to Fig. 20 where in part (a) we see sixteen black trajectories, in (b) fourteen, in (c) twelve and in (d) only six. As we move radially outward from the inner most trajectory in (c) and (d), what is happening is that because this is the higher ϕ case, e is large and hence the peak axial height reached by the particle after bounce is higher than that for (a) and (b). As the axial flow velocity, at a

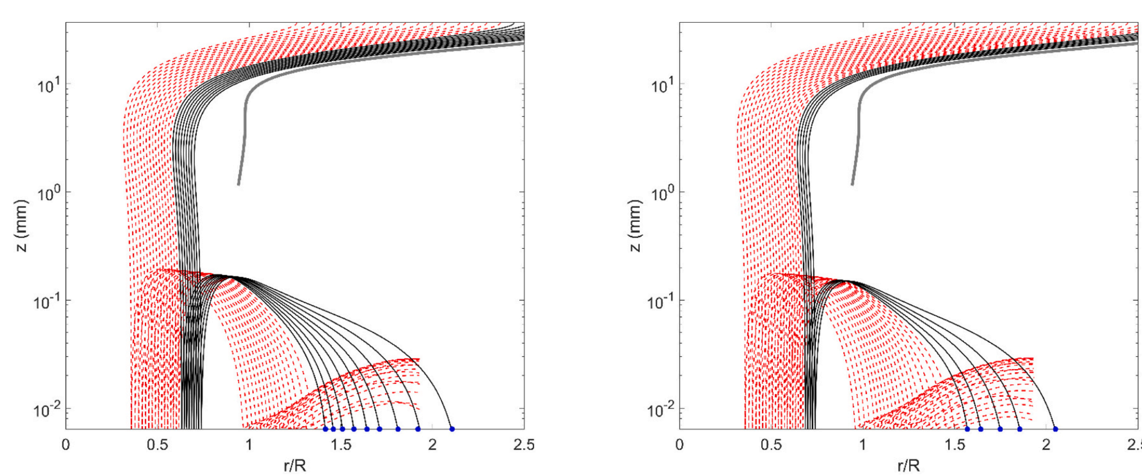

(a) (b)

Fig. 21. Particle trajectories for: (a) $\phi = 0.09$ and (b) $\phi = 0.22$. For both (a) and (b), 25 trajectories are shown which start at equal separation of 0.5 mm from each other at the nozzle inlet starting at r=8.5 mm and moving radially outward. For both (a) and (b), the trajectories in black (solid) are the ones which deposit while the trajectories in red (dashed) are the ones which fail to deposit. The y-axis is logarithmic to more clearly show the trajectories during particle bounce. The thick gray line is the nozzle inner surface. The blue dots represent the final particle deposition locations for the trajectories that deposit. (For interpretation of the references to colour in this figure legend, the reader is referred to the web version of this article.)

given r, increases with z as shown in Fig. 19, the normal velocity of the particle at the second impact is higher for high ϕ than for low ϕ. This implies a greater chance for bounce for high ϕ and leads to a second particle bounce for high ϕ. Due to particles bouncing a second time in (c) and (d), more particle trajectories are exposed to an (r,z) location where the downward fluid velocity is quite high causing them to bounce, yet again, and eventually leave the domain. The limiting starting location at the inlet, of trajectories which deposit to form primary deposits, move further towards the nozzle axis with increasing ϕ, and this causes a decrease in the number of black trajectories in (c) and (d). For the case of the secondary peak, we refer to Fig. 22 where in part (a) we see nine black trajectories and in (b) only five. The same physics presented above is valid for the decrease in the secondary peak for (b) as compared to (a) which is the decrease in critical velocity as change in e is negligible as ϕ increases from 0.09 to 0.22.

The reason that the radial location of the primary and secondary peak is essentially a constant in the experiments and simulations presented here is because of the opposing effects of A and e on the particle bounce characteristics and hence the peak location. A decrease in A causes a decrease in the critical velocity due to which, for constant e, a greater number of trajectories which impact the region of $r/R\sim1$ bounce again and leave the system due to the high axial velocity of the flow near $r/R\sim1$. Hence, for a constant value of e, as A decreases the primary peak moves radially inward and the secondary peak moves radially outward since the particle normal impact velocity v_n peaks near $r/R\sim1$. This is shown in Fig. 23 where v_n at the second impact is plotted versus the impact location for two different values of A, A_1 and A_2, where $A_1>A_2$ and constant e. In these two cases, all trajectories, after leaving the nozzle exit, bounced on the first impact due to particles impacting at near normal incidence. We see that v_n reaches its peak near $r/R\sim1$. Also, as e is the same for both cases, v_n at the second impact and the second impact location remains close to same for both the cases shown in Fig. 23. Hence, the primary and secondary peak location depends on the fate of the trajectories at the second impact. Since $v_{c,1}>v_{c,2}$, more trajectories will bounce after the second impact, in the periphery of $r/R\sim1$, for A_2 compared to A_1. In other words, as A decreases (ϕ increases), the primary peak is whittled away from the right, while secondary peak is whittled away from the left viz. the primary peak moves radially inward while the secondary peak moves radially outward.

At the same time, the decrease in e with ϕ in the lower ϕ region ($\phi=0.09$ to 0.29) causes the particle to lose greater kinetic energy in the normal direction due to which the normal impact velocity after the first bounce decreases. As mentioned earlier, the critical velocity v_c scales with $\frac{A}{e^2}$, which despite the squaring of e, is dominated by A here, due to the very large change in the Hamaker constant A with ϕ compared to the smaller change in e. Hence, for a constant value of A, v_c is essentially constant. Hence, as e decreases, the normal velocities of the trajectories after bounce decreases, causing more trajectories which impact in the periphery of $r/R\sim1$ to deposit on account of these reduced normal impact velocities. Thus, the primary peak moves radially outward away from the nozzle axis, while the secondary peak moves radially inward. This is shown in Fig. 24 where v_n at the second impact is plotted versus the impact location for e_1 and e_2 where $e_1>e_2$ and constant A. In these two cases, all trajectories, after leaving the nozzle exit, bounced on the first impact. We see that for both cases, v_n peaks near $r/R\sim1$. But v_n is lower at all radial locations for e_2 compared to e_1 due to greater loss of normal kinetic energy at the first impact for e_2 as compared to e_1. Since v_c is essentially the same for both cases fewer trajectories will bounce after the second impact, in the periphery of $r/R\sim1$, for e_2 compared to e_1. Thus, as e decreases (ϕ increases), for constant v_c, the primary and secondary peaks move towards each other as the primary peak moves radially outward while the secondary peak moves radially inward.

To summarize, a decrease in A (increase in ϕ), with constant e causes increase in the trajectories that fail to deposit between the depositing black trajectories depicted in Fig. 20 and *Fig. 21* causing the primary and secondary peaks to move away from one another. At the same time, a decrease in e (increase in ϕ), with constant A results in a decrease in the non depositing trajectories between the depositing black trajectories depicted in Fig. 20 and Fig. 21 and the primary and secondary peak move closer to each other. Thus the effect of a decrease in A on the location of the primary and secondary peaks cancels the effect of a decrease in e on the location of the primary and secondary peaks, at least for the range of $\phi=0.09$ to 0.29.

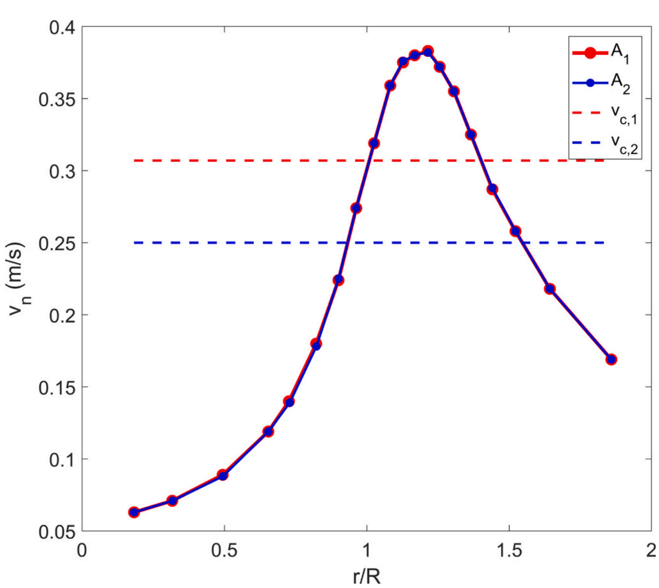

Fig. 23. Normal impact velocity v_n at the second impact versus the impact location for two sets of 20 equally spaced trajectories 1 mm apart starting at r=1 mm corresponding to two different A values, A_1 and A_2 where $A_1>A_2$ and constant e. The red dashed line shows the critical velocity $v_{c,1}$ for the first case while the blue dashed line shows the critical velocity $v_{c,2}$ for the second case. (For interpretation of the references to colour in this figure legend, the reader is referred to the web version of this article.)

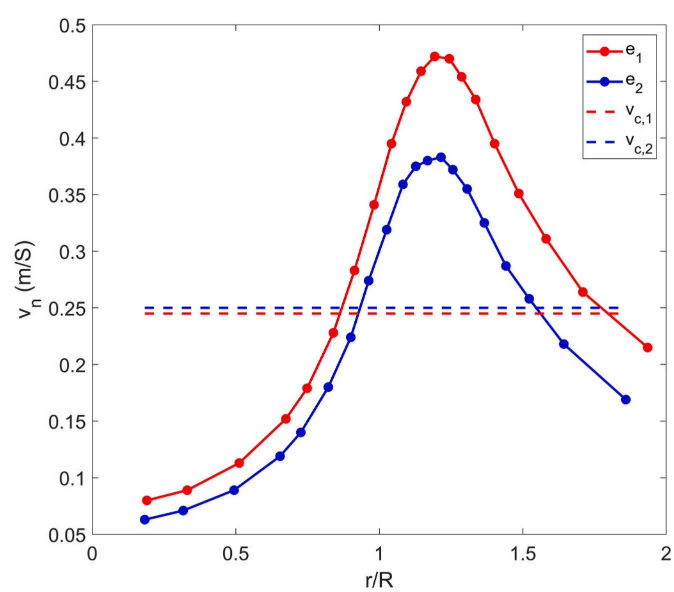

Fig. 24. Normal impact velocity v_n at the second impact versus the impact location for two sets of 20 equally spaced trajectories 1 mm apart starting at r=1 mm corresponding to two different e values, e_1 and e_2 where $e_1>e_2$ and constant A. The red dashed line shows the critical velocity $v_{c,1}$ for the first case while the blue dashed line shows the critical velocity $v_{c,2}$ for the second case. (For interpretation of the references to colour in this figure legend, the reader is referred to the web version of this article.)

Applying the mechanism described above for the high ϕ region where $\phi = 0.30$–0.57, and e increases with ϕ, the peaks will not move closer to each other with decreasing e as was the case in the low ϕ region. This prevents us from explaining the insensitivity of positions of the peaks to ϕ in the high ϕ region. However, the characteristics of the particle trajetcories differ in the high ϕ region. Specifically, the particle trajectories bounce more than twice, losing kinetic energy at each bounce and consequently bouncing to a lower apex after each bounce. While the trajectores whose starting location is radially outward leave the domain after two bounces, the particle trajectories which start very close to the nozzle axis, after the second bounce reach the apex at radial locations which are still well within the nozzle edge $r/R\sim1$. The apex of these trajectories after the second bounce is lower than the apex of the same trajectories after the first bounce and hence they resemble the trajectories for low e cases (low ϕ) wherein they interact with low axial velocity flows and also deposit within the nozzle edge. Hence, for high ϕ region cases, as A decreases (increase in ϕ), its effect of moving the primary peak inward is negated by the innermost particle trajectories which bounce twice and deposit and behave similar to trajectories with low e. Thus the primary peak location remains constant for the high ϕ region cases as well despite the increase in e.

The reason why the secondary peak decreases with ϕ more rapidly than the primary peak in the experiments and simulations presented here is due to the fate of particle trajectories at locations beyond $r/R\sim1$. As seen in Fig. 21, for all ϕ, the trajectories which impact beyond the nozzle edge do so after reaching their apex at $r/R\sim1$ where the axial flow velocity is higher than at $r/R<1$. At the same time, for all ϕ the trajectories which form the primary peak reach their apex at $r/R<1$ as shown in Fig. 20. For high ϕ, particle trajectories bounce twice while for low ϕ particle trajectories bounce once. Therefore, more trajectories reach their apex at $r/R\sim1$ for high ϕ as compared to low ϕ. This qualifies a finite albeit decreasing number of trajectories to reach their apex at $r/R<1$ at high ϕ while the rest reach their apex at $r/R\sim1$. Therefore, at high ϕ there is greater reduction in the depositing trajectories beyond the nozzle edge as compared to depositing trajectories within the nozzle edge, since the critical velocity v_c decreases with ϕ. This translates into a sharper decrease in the secondary peak as compared to the primary peak for high ϕ.

The work presented in this paper is the first of its kind in that it actually simulates the formation of 'halos' in inertial impactors while including elasticity and particle-surface interaction permitting bounce as well as deposition in the simulations. The experiments and simulations presented above were performed using a fixed flow rate (thereby fixed inlet flow velocity). Accordingly, the results and analysis using a fixed flow rate provide significant new knowledge in and of itself. This notwithstanding, for future experiments and simulations the effect of flow velocity on the deposition patterns would be an interesting addition that would broaden the understanding of not just particle-surface interactions, but also the operation of inertial impactors in general. To this effect scaled particle surface density plots were generated for the $\phi = 0.09$ case using a higher and a lower inlet flow velocity than the one considered in the current study. This is shown in Fig. 25. We note that the values of the Hamaker constant and coefficient of restitution used for the new inlet flow velocity cases, shown in Fig. 25 are the same as those determined for $\phi = 0.09$ in the simulations previously presented which may not be the case. The plot in Fig. 25 clearly shows the sensitivity of the particle deposition patterns to the inlet flow velocity and thereby the impactor flow rate.

5. Conclusions

Experiments presented herein demonstrate that, as hypothesized, the collection efficiency of hygroscopic particles in an impactor decreases with relative humidity (ϕ) when the impactor surface is hydrophobic. A novel mechanism for determining surface conditions for particle bounce based on energy conservation was developed and used along with

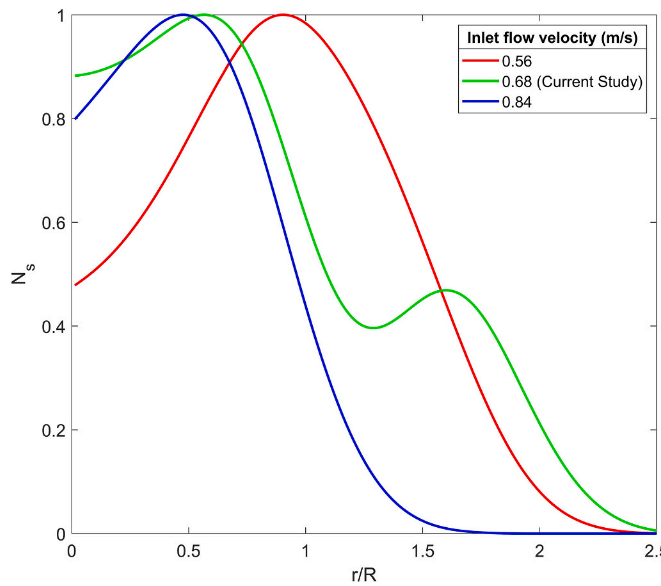

Fig. 25. Plot of N_s versus r/R for $\phi = 0.09$ at three inlet flow velocities: 0.56 m/s, 0.68 m/s, and 0.84 m/s.

particle trajectory simulations to explain the secondary deposits (halos). The mechanism predicts, just as observed in the experiments, that two peaks: a primary peak and a secondary peak occur at fixed radial location. The height of both peaks decreases with relative humidity, more rapidly for the secondary peaks. The mechanism is also used to determine the values Hamaker constant (A) and coefficient of restitution (e) for six reference ϕ cases considered for comparison with the experimental results. The results show that A decreases with increase in ϕ while e remains constant for $\phi = 0.09$ to 0.29 but increases with ϕ from 0.29 to 0.57. This mechanism thus sheds light on the effect of particle elasticity and surface attraction in halo formation which opens door to control this phenomenon in inertial impactors.

Funding

This work was supported by the National Science Foundation [Grant No. 1804304].

CRediT authorship contribution statement

S. Kala: Methodology, Software, Validation, Formal analysis, Investigation, Data curation, Writing – original draft, Visualization. **J.R. Saylor:** Supervision, Funding acquisition, Project administration, Writing – review & editing, Software, Validation, Methodology, Conceptualization.

Declaration of Competing Interest

The authors declare the following financial interests/personal relationships which may be considered as potential competing interests:

Shivuday Kala reports financial support was provided by National Science Foundation.

Data availability

Data will be made available on request.

References

[1] J.F.D.L. Mora, S.V. Hering, N. Rao, P.H. McMurry, Hypersonic impaction of ultrafine particles, J. Aerosol Sci. 21 (1990) 169–187.

[2] P. Kulkarni, P.A. Baron, K. Willeke, Aerosol Measurement: Principles, Techniques, and Applications, third ed., Wiley, 2011.
[3] V.A. Marple, History of impactors - the first 110 years, Aerosol Sci. Technol. 38 (2004) 247–292.
[4] V.A. Marple, D.B. Kittelson, K.L. Rubow, C.P. Fang, Methods for the Selective Sampling of Diesel Particulate in Mine Dust Aerosols, NIOSH Technical Report NTIS: PB 88-130810,, NIOSH, 1986.
[5] T.G. Dzubay, R.K. Stevens, P.L. Haagenson, Composition and origins of aerosol at a forested mountain in soviet Georgia, Environ. Sci. Technol. 18 (1984) 873–883.
[6] P.H. McMurry, X.Q. Zhang, Size distributions of ambient organic and elemental carbon, Aerosol Sci. Technol. 10 (1989) 430–437.
[7] K.Y. Yoon, C.W. Park, J.H. Byeon, J. Hwang, Design and application of an inertial impactor in combination with an ATP bioluminescence detector for in situ rapid estimation of the efficacies of air controlling devices on removal of bioaerosols, Environ. Sci. Technol. 44 (2010) 1742–1746.
[8] R.L. Craig, P.K. Peterson, L. Nandy, Z. Lei, M.A. Hossain, S. Camarena, R. A. Dodson, R.D. Cook, C.S. Dutcher, A.P. Ault, Direct determination of aerosol pH: size-resolved measurements of submicrometer and supermicrometer aqueous particles, Anal. Chem. 90 (2018) 11232–11239.
[9] A. Juozaitis, K. Willeke, S.A. Grinshpun, J. Donnelly, Impaction onto a glass slide or agar versus impingement into a liquid for the collection and recovery of airborne microorganisms, Appl. Environ. Microbiol. 60 (1994) 861–870.
[10] Y.S. Cheng, H.C. Yeh, Particle bounce in cascade impactors, Environ. Sci. Technol. 13 (1979) 1392–1396.
[11] N.A. Esmen, T.C. Lee, Distortion of cascade impactor measured size distribution due to bounce and blow-off, Am. Ind. Hyg. Assoc. J. 41 (1980) 410–419.
[12] T.G. Dzubay, L.E. Hines, R.K. Stevens, Particle bounce errors in cascade impactors, Atmos. Environ. 10 (1976) 229–234.
[13] A.K. Rao, K.T. Whitby, Non ideal collection characteristics of inertial impactors-I. Single stage impactors and solid particles, J. Aerosol Sci. 9 (1978) 77–86.
[14] G.R. Markowski, Reducing blowoff in cascade impactor measurements, Aerosol Sci. Technol. 3 (1984) 431–439.
[15] H.C. Wang, W. John, Comparative bounce properties of particle materials, Aerosol Sci. Technol. 7 (1987) 285–299.
[16] J.R. Turner, S.V. Hering, Greased and oiled substrates as bounce-free impaction surfaces, J. Aerosol Sci. 18 (1987) 215–224.
[17] S.S. Pak, B.Y.H. Liu, K.L. Rubow, Effect of coating thickness on particle bounce in inertial impactors, Aerosol Sci. Technol. 16 (1992) 141–150.
[18] M. Chang, S. Kim, C. Sioutas, Experimental studies on particle impaction and bounce: effects of substrate design and material, Atmos. Environ. 33 (1999) 2313–2322.
[19] M. Kang, H.J. Cho, H. Kwak, K. Park, Evaluation of particle bounce in various collection substrates to be used as vaporizer in aerosol mass spectrometer, Aerosol Sci. Technol. 49 (2015) 332–339.
[20] K.R. May, The cascade impactor: an instrument for sampling coarse aerosols, J. Sci. Instruments 22 (1945) 187.
[21] D.R. Lawson, Impaction surface coatings intercomparison and measurements with cascade impactors, Atmos. Environ. 14 (1980) 195–199.
[22] P. Winkler, Relative humidity and the adhesion of atmospheric particles to the plates of impactors, Aerosol. Sci. 5 (1974) 235–240.
[23] S.W. Stein, B.J. Turpin, X. Cai, P.F. Huang, P.H. Mcmurry, Measurements of relative humidity-dependent bounce and density for atmospheric particles using the DMA impactor technique, Atmos. Environ. 28 (1994) 1739–1746.
[24] A.D. Zimon, Adhesion of Dust and Powder, second ed., Consultants Bureau, New York, 1982.
[25] R. Jones, H.M. Pollock, J.A.S. Cleaver, C.S. Hodges, Adhesion forces between glass and silicon surfaces in air studied by AFM effects of relative humidity, particle size, roughness, and surface treatment, Langmuir 18 (2002) 8045–8055.
[26] J.A.S. Cleaver, J.W.G. Tyrrell, The influence of relative humidity on particle adhesion – a review of previous work and the anomalous behavior of soda-lime glass, KONA Powder Partic. J. 22 (2004) 9–22.
[27] A. Fukunishi, Y. Mori, Adhesion force between particles and substrate in a humid atmosphere studied by atomic force microscopy, Adv. Powder Technol. 17 (2006) 567–580.
[28] K.R. May, Aerosol impaction jets, J. Aerosol Sci. 6 (1975) 403–411.
[29] T. Oodo, Y. Takashima, M. Hanzawa, An experimental study of adhesion of particles with a round nozzle impactor, J. Chem. Eng. Jon. 14 (1981) 76–78.
[30] U. Soysal, E. Géhin, F. Marty, E. Algré, E. Robine, C. Motzkus, Exploring deposition pattern characteristics of aerosols and bioaerosols by inertial impaction for the development of real-time silicon MEMS mass detection systems, Aerosol Sci. Technol. 55 (2021) 414–422.
[31] V. Sethi, W. John, Particle impaction patterns from a circular jet, Aerosol Sci. Technol. 18 (1993) 1–10.
[32] J.Q. Feng, A computational study of particle deposition patterns from a circular laminar jet, J. Appl. Fluid Mech. 10 (2016) 1001–1012.
[33] B. Dahneke, The capture of aerosol particles by surfaces, J. Colloid Interface Sci. 37 (1971) 342–353.
[34] F. Loeffler, Adhesion probability in fiber filters, Clean Air. 8 (1974) 75–78.
[35] C. Davies, Definitive equations for the fluid resistance of spheres, Proc. Phys. Soc. 57 (1945) 259–270.
[36] E.M. Lifshitz, Soviet. Phys. JETP (Engl. Transl.) 2 (1956) 73–83.
[37] J.N. Israelachvili, Intermolecular and Surface Forces, second ed., Academic Press, London, 1992.
[38] National Toxicology Program, Institute of Environmental Health Sciences, National Institutes of Health (NTP), National Toxicology Program Chemical Repository Database, 1992.
[39] S. Fredericks, J.R. Saylor, Ring-shaped deposition patterns in small nozzle-to-plate distance impactors, Aerosol Sci. Technol. 52 (2017) 30–37.
[40] J.H. Bell, R.D. Mehta, Contraction Design for Small Low-Speed Wind Tunnels, Technical report, NASA, 1988.
[41] S. Kala, J.R. Saylor, Factors affecting the diameter of ring-shaped deposition patterns in inertial impactors having small S/W ratios, Aerosol Sci. Technol. 56 (2022) (2022) 234–246.
[42] R.S. Bradley, Philos. Mag. 13 (1932) 853–862.
[43] H.C. Hamaker, Physica 4 (1937) 1058–1072.
[44] M. Elimelech, J. Gregory, X. Jia, R.A. Williams, Particle Deposition & Aggregation Measurement, Modelling and Simulation, second ed., Butterworth-Heinemann, 1998.
[45] R.N. Berglund, Benjamin Y.H. Liu, Generation of monodisperse aerosol standards, Environ. Sci. Technol. 7 (1973) 147–153.
[46] TSI Model 3450 Vibrating Orifice Aerosol Generator Instruction Manual, 2002 pp. L:4–7.
[47] Z. Qin, R.H. Pletcher, Particle impact theory including surface asperity deformation and recovery, J. Aerosol Sci. 42 (2011) 852–858.
[48] X. Li, M. Dong, D. Jiang, S. Li, Y. Shang, The effect of surface roughness on normal restitution coefficient, adhesion force and friction coefficient of the particle-wall collision, Powder Technol. 362 (2011) 17–25.
[49] C.S. Sandeep, L. Luo, K. Senetakis, Effect of grain size and surface roughness on the normal coefficient of restitution of single grains, Materials (Basel) 13 (2020) 814.
[50] A. Ghanbarzadeh, A. Hassanpour, A. Neville, A numerical model for calculation of the restitution coefficient of elastic-perfectly plastic and adhesive bodies with rough surfaces, Powder Technol. 345 (2019) 203–212.
[51] M. Xu, K. Willeke, P. Biswas, S.E. Pratsinis, Impaction and rebound of particles at acute incident angles, Aerosol Sci. Technol. 18 (1993) 143–155.
[52] J. Xie, Z. Zhu, T. Yang, M. Dong, R. Li, The effect of incident angle on the rebound behavior of micro-particle impacts, J. Aerosol Sci. 155 (2021), 105778.
[53] W. Tabakoff, M.F. Malak, Laser measurements of Fly ash rebound parameters for use in trajectory calculations, J. Turbomach. 109 (1987) 535–540.